Chinese Chemical Letters 32 (2021) 2484–2488

Contents lists available at ScienceDirect

Chinese Chemical Letters

journal homepage: www.elsevier.com/locate/cclet

Communication

3D ordered macro-/mesoporous Ni_xCo_{100-x} alloys as high-performance bifunctional electrocatalysts for overall water splitting

Chenhui Niu[a], Yixin Zhang[a], Jing Dong[a], Ruixue Yuan[a], Wei Kou[a], Lianbin Xu[a,b,*]

[a] State Key Laboratory of Organic–Inorganic Composites, Beijing University of Chemical Technology, Beijing 100029, China
[b] Research Center of the Ministry of Education for High Gravity Engineering and Technology, Beijing University of Chemical Technology, Beijing 100029, China

ARTICLE INFO

Article history:
Received 15 October 2020
Received in revised form 20 November 2020
Accepted 23 December 2020
Available online 29 December 2020

Keywords:
Macro-/mesoporous structure
Ni-Co alloys
Dual-templating technique
Electrocatalysts
Water splitting

ABSTRACT

Electrochemical water splitting is a facile and effective route to generate pure hydrogen and oxygen. However, the sluggish kinetics of hydrogen evolution reaction (HER) and especially oxygen evolution reaction (OER) hinder the water splitting efficiency. Meanwhile, the high-cost of noble-metal catalysts limit their actual application. It is thus highly urgent to exploit an economical and earth-abundant bifunctional HER and OER electrocatalyst to simplify procedure and reduce cost. Herein, we synthesize the three-dimensionally ordered macro-/mesoporous (3DOM/m) Ni_xCo_{100-x} alloys with distinctive structure and large surface area *via* a dual-templating technique. Among them, the 3DOM/m $Ni_{61}Co_{39}$ shows the lowest overpotentials of 121 mV and 241 mV at 10 mA/cm^2 for HER and OER, respectively. Furthermore, when employed for water splitting, the $Ni_{61}Co_{39}$ only requires 1.60 V to approach 10 mA/cm^2 and presents excellent stability. These encouraging performances of the $Ni_{61}Co_{39}$ render it a promising bifunctional catalyst for overall water splitting.

Hydrogen with high energy density and renewable character has been viewed as one of the sustainable and promising energy carriers. Electrochemical water splitting is an effective and prospective strategy to generate hydrogen, which involves the oxygen evolution reaction (OER) and the hydrogen evolution reaction (HER) [1,2]. However, besides the HER, OER normally requires a higher potential and possesses a complicated reaction mechanism leading to sluggish kinetic process, which restrict the practical utilization in water splitting. The practical operating potential for water splitting is typically 1.8–2.0 V, which is much higher than the theoretical value (1.23 V) [3]. The high-performance bifunctional electrocatalyst can reduce the overpotentials for both HER and OER and thus enhance the efficiency for water splitting. Currently, the noble metals and their oxides have been utilized as efficient catalysts to enhance the electrocatalytic performance [4]. However, the high cost, scarcity in the earth and lower stability hinder their industrialization [5]. It is important to develop the electrocatalysts with low cost, high-performance and excellent stability for water splitting.

Ni and Ni-based catalysts have attracted widespread interests due to their cost-effectiveness, low overpotential, and excellent stability for HER [6,7] and OER [8–10]. Interestingly, compared with pure Ni catalysts, Ni-based alloy catalysts have presented the enhanced electrolytic efficiency, which may be due to the electronic structures and synergetic combination of different metals [11]. Specifically, Ni-Co alloys with various structures have been reported for water splitting because of their intrinsic corrosion stability and abundant valence states, such as nanothorn arrays [12], nanowires [13], hollow microcuboids [14], and hierarchical three-dimensional (3D) structure [15]. Among them, the 3D hierarchical porous structural material exhibits remarkable catalytic activity owing to relatively high surface area and good mass/charge transmission capabilities [16]. For example, Zhou *et al.* reported the hierarchical porous Co-based phosphate 3D networks in which the overpotential for OER is 315 mV at 10 mA/cm^2 with a Tafel slope of 33 mV/dec [17]. Li *et al.* prepared spinel $NiCo_2O_4$ 3D nanoflowers supported on graphene nanosheets, the Tafel slope is 137 mV/dec and the onset potential is 1.50 V for OER [18]. Unfortunately, most of the reported 3D hierarchical porous materials show disordered macro-/mesoporous structure and the morphology is difficult to control, which could hinder the transfer through the porous structures and limit further performance promotion. However, the ordered mesopores can provide catalysts with superb access to more active sites, the

* Corresponding author at: State Key Laboratory of Organic–Inorganic Composites, Beijing University of Chemical Technology, Beijing 100029, China.
E-mail address: xulb@mail.buct.edu.cn (L. Xu).

https://doi.org/10.1016/j.cclet.2020.12.045
1001-8417/

macropores can speed up mass/electron transfer, and the high stable 3D ordered porous network enable catalysts to exhibit a long-term stability [19,20]. To this end, designing the 3D ordered macro-/mesoporous materials is urgently imperative.

Herein, the 3D ordered macro-/mesoporous Ni_xCo_{100-x} alloys (3DOM/m Ni_xCo_{100-x}) were prepared *via* a dual-templating method and they were evaluated as high-performance bifunctional catalysts for HER and OER for the first time. The optimum 3DOM/m $Ni_{61}Co_{39}$ catalyst requires 121 mV and 241 mV to reach 10 mA/cm^2 in terms of HER and OER, respectively. Meanwhile, the $Ni_{61}Co_{39}$ catalyst is applied as both cathode and anode in water electrolysis, only 1.60 V is afforded at 10 mA/cm^2. The results of this study confirm that coupling hierarchical porous nanostructures with the synergistic effect of alloying could lead to exceptional electrocatalytic activity for water splitting.

Fig. S1 (Supporting information) demonstrates the process for preparing 3DOM/m Ni_xCo_{100-x}. Polymethyl methacrylate (PMMA) spheres were firstly synthesized *via* previously reported method [21]. PMMA opal with highly ordered close-packed PMMA spheres was obtained by self-assembly. Then, the lyotropic liquid crystals (LLC) [22] containing Ni^{2+}/Co^{2+} with different ratios and nonionic surfactant Brij 58 ($C_{16}H_{33}(OCH_2CH_2)_{20}OH$) were immersed into the intervals of PMMA. Finally, after the reduction of Ni^{2+} and Co^{2+} with dimethylamine borane (DMAB) and then removal of the PMMA, the 3DOM/m Ni_xCo_{100-x} alloys were fabricated.

The Ni-Co composition percentages of the 3DOM/m Ni_xCo_{100-x} samples tested by inductively coupled plasma (ICP) are listed in Table S1 (Supporting information). The transmission electron microscopy (TEM) and scanning electron microscopy (SEM) were used to study the internal structure and morphology of the $Ni_{61}Co_{39}$. The SEM images of the $Ni_{61}Co_{39}$ alloy (Fig. 1a) preserve the highly ordered 3D macroporous structure, which is the inverse structure of the original PMMA template (Fig. S2a in Supporting information). The macroporous diameter is around 340 nm which is in conformity with the size of the PMMA template. The TEM images (Fig. 1b) also show well-defined 3D porous structure and the size of macropores is around 340 nm. From the higher magnification image shown in the inset of Fig. 1b, the mesoporous size is in a range of 3−5 nm. In addition, the TEM images of $Ni_{61}Co_{39}$ at different orientations are displayed in Figs. S2b-d, respectively (Supporting information). Fig. S3 (Supporting information) shows the TEM images of 3DOM/m Ni_xCo_{100-x} catalysts with different ratios of nickel and cobalt. The $Ni_{61}Co_{39}$ shows the clearer and higher ordered structure. Moreover, with the increasing of Co ions, mesoporous structure of samples becomes disordered, which may be due to the activity of Co is less than Ni for anodic oxidation of DMAB [23]. Furthermore, the elemental mapping of the 3DOM/m $Ni_{61}Co_{39}$ (Fig. S4 in Supporting information) shows homogeneous distribution of Ni and Co across the selected area.

The textural properties of 3DOM/m $Ni_{61}Co_{39}$ were analyzed by N_2 adsorption-desorption measurement (Fig. 2a). The isotherm exhibits type IV, proving the presence of mesoporous structure

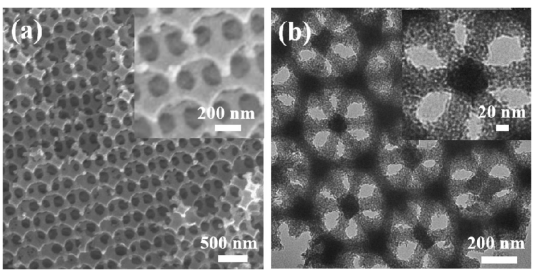

Fig. 1. (a) SEM and (b) TEM images for the $Ni_{61}Co_{39}$, inset: magnified image.

[24]. The Brunauer-Emmett-Teller (BET) specific surface area of the $Ni_{61}Co_{39}$ is 115 m^2/g with the total pore volume is 0.21 cm^3/g. With respect to the Barrett-Joyner-Halenda (BJH) distribution curve, it shows a narrow peak at 3.8 nm suggesting the uniform mesopore distribution, which is in concordance with the TEM. X-Ray Diffraction (XRD) can explore the crystal phase of $Ni_{61}Co_{39}$ (Fig. 2b). The broad peak at about $2\theta = 45^\circ$ indicates that the catalyst exists in an amorphous-like state [25]. Fig. S5 (Supporting information) show the XRD patterns of 3DOM/m Ni_xCo_{100-x} catalysts. With the Co content increases, the intensity of the broad peak at around 45° drops [26]. No peaks for the oxidation states of Ni and Co are observed in the XRD patterns, indicating that Ni_xCo_{100-x} alloys mainly exist in the metallic state. The small-angle XRD pattern (inset in Fig. 2b) presents a peak at $2\theta = 1.3^\circ$ which further proves the existence of ordered mesostructure [25]. The selected-area electron diffraction (SAED) pattern shows halo rings, implying the existence of amorphous state, which is in conformity with the XRD [26].

We first investigated the HER performance for 3DOM/m Ni_xCo_{100-x} catalysts and 20% Pt/C for comparison in 1.0 mol/L KOH. The cyclic voltammetry (CV) was run for 30 cycles to stabilize the system before recording the data. The CV curve (Fig. S6 in Supporting information) shows no redox peaks, indicating no additional reduction step occurs [27]. From linear sweep voltammetry (LSV) curves in Fig. 3a, the overpotential required for $Ni_{61}Co_{39}$ catalyst to reach 10 mA/cm^2 is just 121 mV, better than the Ni (172 mV), $Ni_{73}Co_{27}$ (146 mV), $Ni_{49}Co_{51}$ (161 mV), $Ni_{15}Co_{85}$ (250 mV), and Co (294 mV).

The HER catalytic kinetics of all samples were probed by Tafel plots in Fig. 3b. The Tafel slope for 20% Pt/C is consistent with the reported results (31 mV/dec) [28]. The slope for $Ni_{61}Co_{39}$ is 41 mV/dec, which is superior to electrodes for Ni, $Ni_{73}Co_{27}$, $Ni_{49}Co_{51}$, $Ni_{15}Co_{85}$, and Co with a slope of 52, 47, 49, 68, and 77 mV/dec, respectively. It is worth noting that the Tafel reaction is dominated by rate-limiting step in alkaline electrolyte. The Tafel slope of 41 mV/dec indicates that $Ni_{61}Co_{39}$ follows a Volmer-Heyrovsky mechanism for HER [29] (see Supporting information for details).

Electrochemical impedance spectroscopy (EIS) was conducted to research the charge transfer kinetics of all samples for HER. The Nyquist curves (Fig. 3c) reveal that the impedance value of $Ni_{61}Co_{39}$ is 4.5 Ohms, indicating that $Ni_{61}Co_{39}$ possesses the highest charge transfers effectiveness [30]. The turnover frequency (TOF) can assess the intrinsic properties of samples [31]. The $Ni_{61}Co_{39}$ catalyst has the highest TOF which is around 4.3×10^{-4} s^{-1} at η = 10 mV (Table S2 in Supporting information).

Stability is also an important evaluation factor for catalysts. From Fig. 3d, the LSV curve of the $Ni_{61}Co_{39}$ catalyst is basically unchanged before and after the 2000 CV cycles. The inset in Fig. 3d shows the chronopotentiometry curve. At a stable current density of 10 mA/cm^2, the activity of $Ni_{61}Co_{39}$ electrode decreases slightly (∼6.9%) after 25 h of continuous operation. Meanwhile, after the stability test, there are no obvious changes of morphology and porous structure from the TEM observation (Fig. S7 in Supporting information), suggesting the remarkable stability for HER in alkaline solution.

Prior to the LSV measurement for OER, the CV (Fig. S8 in Supporting information) was tested to activate the catalysts. The redox peak between 1.0–1.4 V is assigned to Ni^{2+} and Co^{2+} [32]. The 3DOM/m $Ni_{61}Co_{39}$ with well-ordered macro-/mesoporous structure shows the best OER activities and the overpotential is 241 mV at 10 mA/cm^2. However, the Ni, $Ni_{73}Co_{27}$, $Ni_{49}Co_{51}$, $Ni_{15}Co_{85}$, Co and RuO_2 require higher overpotentials of 297, 264, 282, 306, 333 and 305 mV, respectively (Fig. 3e). The Tafel slope of $Ni_{61}Co_{39}$ is 44 mV/dec, which is lower than that of other Ni_xCo_{100-x} catalysts and even RuO_2 (Fig. 3f), proving the favorable OER kinetics for $Ni_{61}Co_{39}$. Fig. 3g displays the EIS for the 3DOM/m Ni_xCo_{100-x} catalysts and

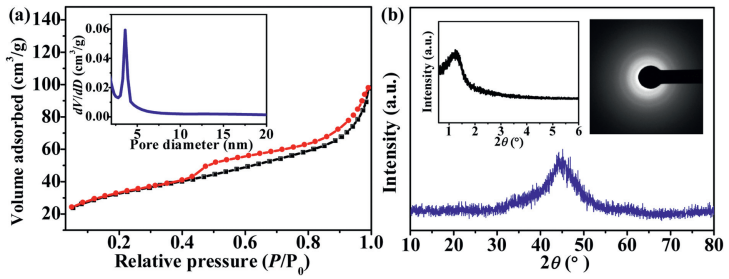

Fig. 2. (a) N_2 adsorption-desorption isotherm of $Ni_{61}Co_{39}$ catalyst, inset: Pore size distribution curve. (b) The XRD pattern for the $Ni_{61}Co_{39}$, inset: Corresponding selected-area electron diffraction (SAED) and small-angle XRD.

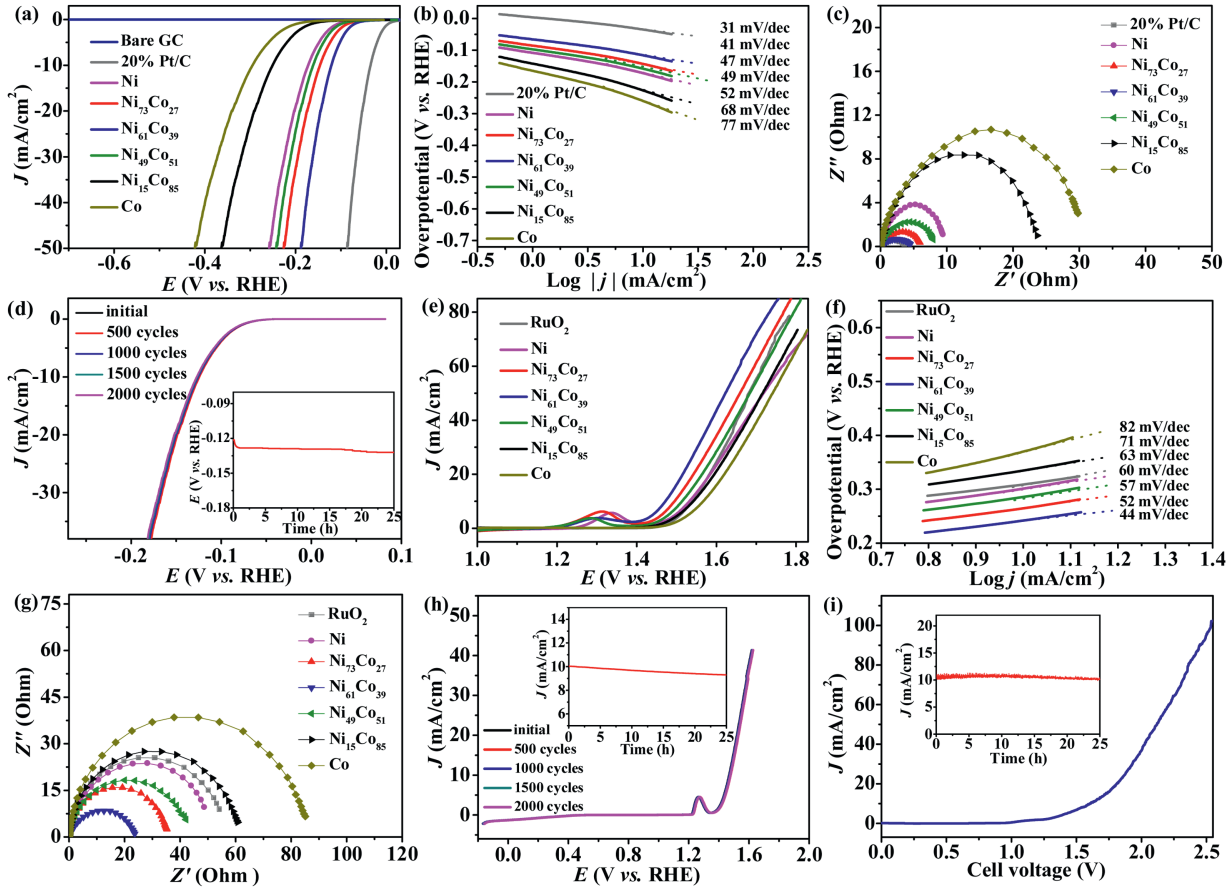

Fig. 3. (a, b) LSV and Tafel curves for the Ni_xCo_{100-x} catalysts and 20% Pt/C for HER. (c) The Nyquist curves of catalysts recorded at -0.10 V. (d) LSV curves of $Ni_{61}Co_{39}$ catalyst for the HER initially and after every 500 cycles, inset: The chronopotentiometry curve obtained from continuous testing of $Ni_{61}Co_{39}$ catalyst for 25 h at 10 mA/cm^2. (e, f) LSV and Tafel curves for the Ni_xCo_{100-x} catalysts and RuO_2 for OER. (g) EIS of catalysts recorded at 1.70 V. (h) LSV curves of $Ni_{61}Co_{39}$ catalyst for the OER initially and after every 500 cycles, inset: The chronoamperometry curve obtained from continuous stability testing of $Ni_{61}Co_{39}$ catalyst for 25 h at 1.47 V *vs.* RHE. (i) LSV curve of water splitting for the $Ni_{61}Co_{39}$ catalyst, inset: stability test at 1.60 V *vs.* RHE.

RuO_2. The $Ni_{61}Co_{39}$ electrode has the smallest semicircle diameter (23 Ohms), manifesting the lowest resistance and good mass transport. In addition, the $Ni_{61}Co_{39}$ catalyst showed the highest TOF (5.8×10^{-4} s^{-1}). The relative data are listed in Table S3 (Supporting information).

The stability for the $Ni_{61}Co_{39}$ is tested by 2000 cycles of CV. The LSV curve of $Ni_{61}Co_{39}$ (Fig. 3h) was almost overlapped with the original one, confirming the good stability, which is significant in actual appliance. Moreover, the time-dependency of catalytic overpotential was performed by the chronoamperometry method at 1.47 V *vs.* RHE in 1.0 mol/L KOH for 25 h (inset of Fig. 3h). The curve of the $Ni_{61}Co_{39}$ shows negligible decay (~8.0%), implying that the electrode has good stability in the electrochemical process, which may be ascribed to the negligible deformation of the interconnected 3D porous structure after the test (Fig. S9 in Supporting information).

Considering that the 3DOM/m $Ni_{61}Co_{39}$ electrode has fast catalytic kinetics for both HER and OER under alkaline environment, this electrode could be used as anode and cathode for water electrolysis. It can be observed from Fig. 3i that $Ni_{61}Co_{39}$ electrode requires 1.60 V at 10 mA/cm^2. This value is close to previously reported RuO_2||Pt/C electrode (1.55 V) [33], Co-Ni-P (1.61 V) [34] and even favorable to $NiCo_2O_4$ hollow microcuboids (1.65 V) [14], porous $NiCo_2N$ (1.70 V) [35], *etc.* (Table S4 in Supporting information). The electrocatalytic stability in a two-cell electrode was studied using a chronoamperometry test at 1.60 V *vs.* RHE, and

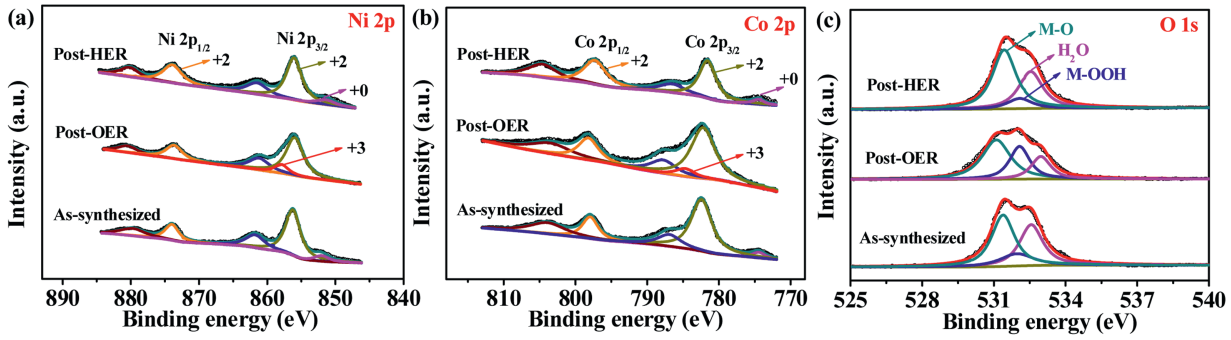

Fig. 4. XPS spectra of the as-synthesized, post-HER and post-OER samples. (a) Ni 2p, (b) Co 2p, (c) O 1s.

the result displays in the inset of Fig. 3i. The $Ni_{61}Co_{39}$ catalyst exhibits high stability with ~7.4% current density decay for 25 h water electrolysis. The results demonstrate that the 3DOM/m $Ni_{61}Co_{39}$ electrode can be effectively utilized as bifunctional HER and OER electrocatalyst for water splitting.

The surface composition and elemental state of $Ni_{61}Co_{39}$ were explained by X-ray photoelectron spectroscopy (XPS). Fig. S10 (Supporting information) shows the XPS survey spectra of the $Ni_{61}Co_{39}$ catalyst which show the presence of Ni, Co and O elements on the surface of as-synthesized sample. The high resolution XPS spectrum of Ni 2p for as-synthesized $Ni_{61}Co_{39}$ is shown in Fig. 4a. There are two main peaks appear at 856.2 eV and 874.0 eV, which are ascribed to Ni $2p_{3/2}$ and Ni $2p_{1/2}$, respectively [36]. At the same time, two broad satellite peaks at 860.9 and 880.2 eV suggest the presence of Ni^{2+}. The peak at 852.1 eV reveals the sample contains metallic Ni^0 [37]. The Co 2p (Fig. 4b) shows two main peaks (781.7 eV and 797.0 eV) belonging to Co $2p_{3/2}$ and Co $2p_{1/2}$ and two satellite peaks (785.7 and 802.9 eV), which are assigned to Co^{2+} [38]. The peak at 774.4 eV is attributed to zero valence of Co [39]. The detected divalent oxide peaks of Ni and Co may be caused by the partial oxidation on the catalyst surface in the preparation process and atmospheric exposure. The high resolution XPS spectrum of O 1s (Fig. 4c) shows three peaks at 531.1 eV, 531.9 eV and 532.6 eV which are M—O peak (M=Ni, Co), M-OOH peak and the oxygen species in the surface-adsorbed H_2O molecule, respectively [40].

The XPS spectra of $Ni_{61}Co_{39}$ catalyst after the HER and OER stability tests (Fig. 4) are also analyzed. After the HER, the XPS spectra of Ni 2p and Co 2p are similar to those of the original sample, with the same oxidation/metallic states on the catalyst surface. And the XPS spectra of O 1s before and after the HER test also indicate the formation M—O bond evidenced by the peaks at 531.1 eV. Moreover, it is commonly accepted that the HER process consists of three possible steps (see Supporting information for details) [41]. The initial stage is the Volmer reaction, followed by either Heyrovsky reaction or Tafel reaction. A lot of work has demonstrated that MO accelerates the Volmer step, while the metallic species is beneficial to the Heyrovsky or Tafel step [42,43]. On the MO/M interface, the OH^- from H_2O dissociation might preferentially adhere to the MO surface since it has a strong electrostatic affinity to M^{2+} component and there are more unfilled d orbitals in M^{2+} than M^0, while a nearby M site would promote H adsorption, giving MO/M the synergistic catalytic activity for HER [44]. Thus, the MO/M might be the synergistically active sites for HER electrocatalysis.

After the OER stability test, the metallic phases Ni^0 (852.1 eV) and Co^0 (774.4 eV) disappeared, suggesting that the surface metallic Ni and Co were oxidized. Notably, new peaks at 858.2 eV and 784.6 eV are assigned to trivalent NiOOH and CoOOH, respectively, which are key OER intermediates formed on the surface of $Ni_{61}Co_{39}$ [45,46]. This result can be confirmed by the high-resolution O 1s XPS spectra. After the OER, the intensity of M–OOH peak (531.9 eV) increased significantly. It is generally believed that the Ni/Co—OOH are the real active phases for OER [47].

It is anticipated that the outstanding electrochemical activities of the 3DOM/m $Ni_{61}Co_{39}$ could be originated from its distinct 3D hierarchical macro-/mesoporous structure and the synergetic combination of Ni and Co. (1) The ordered mesopores increase the surface area of $Ni_{61}Co_{39}$ catalyst, thereby exposing more catalytically active sites, while macropores can accelerate the diffusion of molecules/ions to the active sites, facilitate the electron transport rates and boost the utilization efficiency [48,49]. (2) Alloying Ni with appropriate amount Co could reduce the overpotentials and improving the catalytic activity for both HER and OER and thus accelerating the efficiency of overall water splitting [50,51], but the excessive Co could lead to the destruction of ordered mesoporous structure and decrease of synergism effect [23]. (3) Due to their amorphous structures with short range order, the synthesized amorphous state catalysts may be able to expose the active sites in the bulk through electrochemically activation, resulting in an increase in the number of active sites, thereby enhancing the catalytic performance [52].

In this paper, noble-metal-free 3DOM/m Ni_xCo_{100-x} alloys have been prepared *via* a facile dual-templating method where PMMA opal and the surfactant Brij 58 as macropore template and mesopore directing agent, respectively. Because of the synergistic properties of bimetals, rich active sites exposure and distinctive mass transport ability derived from the unique hierarchical macro-/mesoporous architecture, the optimal $Ni_{61}Co_{39}$ catalyst exhibits superior electrocatalytic performance with the overpotentials of 121 mV and 241 mV at 10 mA/cm^2 for HER and OER, respectively. Furthermore, $Ni_{61}Co_{39}$ electrode only requires 1.60 V at 10 mA/cm^2 in water splitting system. The remarkable electrocatalytic activity indicate that the $Ni_{61}Co_{39}$ catalyst may be a promising candidate to replace noble-metal catalysts. The uniform 3D macro-/mesoporous structure might offer a new strategy for designing Ni-based alloy catalysts as highly active electrodes for various electrochemical applications, such as electrocatalysis, batteries and supercapacitors.

Declaration of competing interest

The authors declare that they have no known competing financial interests or personal relationships that could have appeared to influence the work reported in this paper.

Acknowledgment

The work was financially supported by the National Natural Science Foundation of China (No. 21676018 and 51172014).

Appendix A. Supplementary data

Supplementary material related to this article can be found, in the online version, at doi:https://doi.org/10.1016/j.cclet.2020.12.045.

References

[1] M.I. Jamesh, J. Power Sources 333 (2016) 213–236.
[2] H.T. Wang, H.W. Lee, Y. Deng, et al., Nat. Commun. 6 (2015) 7261.
[3] J. Yin, Y.X. Li, F. Lv, et al., Adv. Mater. 29 (2017) 1704681.
[4] Z.W. Zhuang, Y. Wang, C.Q. Xu, et al., Nat. Commun. 10 (2019) 4875.
[5] K. Lan, X. Wang, H.D. Yang, et al., ChemElectroChem 5 (2018) 2256–2262.
[6] D. Ansovini, C.J.J. Lee, C.S. Chua, et al., J. Mater. Chem. A 4 (2016) 9744–9749.
[7] X. Jian, S. Li, J.Z. Liu, et al., ChemElectroChem 6 (2019) 5407–5412.
[8] D. Friebel, M.W. Louie, M. Bajdich, et al., J. Am. Chem. Soc. 137 (2015) 1305–1313.
[9] G.T. Fu, X.X. Yan, Y.F. Chen, et al., Adv. Mater. 30 (2018) 1704609.
[10] C. Yu, J.J. Lu, L. Luo, et al., Electrochim. Acta 301 (2019) 449–457.
[11] Q. Zhang, P.S. Li, D.J. Zhou, et al., Small 13 (2017) 1701648.
[12] Y.Q. Ji, J.Q. Xie, Y. Yang, et al., Chin. Chem. Lett. 31 (2020) 855–858.
[13] A. Sivanantham, P. Ganesan, S. Shanmugam, Adv. Funct. Mater. 26 (2016) 4661–4672.
[14] X.H. Gao, H.X. Zhang, Q.G. Li, et al., Angew. Chem. Int. Ed. 55 (2016) 6290–6294.
[15] X.W. Wei, X.M. Zhou, K.L. Wu, Y. Chen, CrystEngComm 13 (2011) 1328–1332.
[16] W. Kou, Y.X. Zhang, J. Dong, et al., ACS Appl. Energy Mater. 3 (2020) 1875–1882.
[17] Y. Zhou, H.C. Zeng, Small 14 (2018) 1704403.
[18] Z.S. Li, B.L. Li, J.M. Chen, Q. Pang, P.K. Shen, Int. J. Hydrogen Energy 44 (2019) 16120–16131.
[19] J.F. Zhang, Y. Li, T.Y. Zhu, et al., ACS Appl. Mater. Interfaces 10 (2018) 31330–31339.
[20] A.M. Lázaro, A.R. Zavala, F.I.E. Lagunes, et al., J. Power Sources 412 (2019) 505–513.
[21] R.C. Schroden, M. Al-Daous, C.F. Blanford, A. Stein, Chem. Mater. 14 (2002) 3305–3315.
[22] G.S. Attard, P.N. Bartlett, N.R.B. Coleman, et al., Science 278 (1997) 838–840.
[23] Y. Yamauchi, T. Yokoshima, T. Momma, T. Osaka, K. Kuroda, J. Mater. Chem. 14 (2004) 2935–2940.
[24] K.S.W. Sing, D.H. Everett, R.A.W. Haul, et al., Pure Appl. Chem. 57 (1985) 603–619.
[25] Y. Yamauchi, T. Yokoshima, H. Mukaibo, et al., Chem. Lett. 33 (2004) 542–543.
[26] Y. Yamauchi, M. Komatsu, M. Fuziwara, et al., Angew. Chem. Int. Ed. 48 (2009) 7792–7797.
[27] C. Tang, N.Y. Cheng, Z.H. Pu, W. Xing, X.P. Sun, Angew. Chem. Int. Ed. 54 (2015) 9351–9355.
[28] H.L. Lin, Z.P. Shi, S.N. He, et al., Chem. Sci. 7 (2016) 3399–3405.
[29] N. Krstajic, M. Popovic, B. Grgur, M. Vojnovic, D. Sepa, J. Electroanal. Chem. 512 (2001) 16–26.
[30] L. Negahdar, F. Zeng, S. Palkovits, C. Broicher, R. Palkovits, ChemElectroChem 6 (2019) 5588–5595.
[31] J.Y. Xu, T.F. Liu, J.J. Li, et al., Energy Environ. Sci. 11 (2018) 1819–1827.
[32] X. Xu, H.F. Liang, F.W. Ming, et al., ACS Catal. 7 (2017) 6394–6399.
[33] F.W. Ming, H.F. Liang, H.H. Shi, et al., J. Mater. Chem. A 4 (2016) 15148–15155.
[34] C. Huang, T. Ouyang, Y. Zou, N. Li, Z.Q. Liu, J. Mater. Chem. A 6 (2018) 7420–7427.
[35] Y.Q. Wang, B.H. Zhang, W. Pan, H.Y. Ma, J.T. Zhang, ChemSusChem 10 (2017) 4170–4177.
[36] T.T. Sun, L.B. Xu, Y.S. Yan, et al., ACS Catal. 6 (2016) 1446–1450.
[37] X.E. Liu, W. Liu, M. Ko, et al., Adv. Funct. Mater. 25 (2015) 5799–5808.
[38] S. Rafai, C. Qiao, Z.T. Wang, et al., ChemElectroChem 6 (2019) 5469–5478.
[39] B. Subramanya, Y. Ullal, S.U. Shenoy, D.K. Bhat, A.C. Hedge, RSC Adv. 5 (2015) 47398–47407.
[40] A. Jayakumar, R.P. Antony, R.H. Wang, J.M. Lee, Small 13 (2017) 1603102.
[41] X.D. Zhang, Y. Li, Y.K. Guo, et al., Int. J. Hydrogen Energy 44 (2019) 29946–29955.
[42] L. Zhao, Y. Zhang, Z.L. Zhao, et al., Natl. Sci. Rev. 7 (2020) 27–36.
[43] X.E. Liu, W. Liu, M.S. Park, et al., Adv. Funct. Mater. 25 (2015) 5799–5808.
[44] M. Gong, W. Zhou, M.C. Tsai, et al., Nat. Commun. 5 (2014) 4695.
[45] Q. Zhang, C. Ye, X.L. Li, et al., ACS Appl. Mater. Interfaces 10 (2018) 27723–27733.
[46] I.H. Kwak, H.S. Im, D.M. Jang, et al., ACS Appl. Mater. Interfaces 8 (2016) 5327–5334.
[47] C.L. Xiao, Y.B. Li, X.Y. Lu, C. Zhao, Adv. Funct. Mater. 26 (2016) 3515–3523.
[48] C.W. Zhang, H. Yang, T.T. Sun, et al., J. Power Sources 245 (2014) 579–582.
[49] J. Dong, T.T. Sun, S.Y. Li, et al., J. Colloid Interface Sci. 554 (2019) 177–182.
[50] R.P. Antony, A.K. Satpati, K. Bhattacharyya, B.N. Jagatap, Adv. Mater. Interfaces 3 (2016) 1600632.
[51] S. Barwe, C. Andronescu, E. Vasile, J. Masa, W. Schuhmann, Electrochem. Commun. 79 (2017) 41–45.
[52] W.Z. Cai, R. Chen, H.B. Yang, et al., Nano Lett. 20 (2020) 4278–4285.